Interpretable and physics-supported machine learning model for sound transmission loss analysis

B. Z. Cunha [1,2]**, M. Ichchou** [1]**, C. Droz** [3]**, A.-M. Zine** [4]**, S. Foulard** [2]
[1] Ecole Centrale Lyon, Laboratory of Tribology and Dynamics of Systems,
Ecully, 69130, France
e-mail: **barbara.zaparoli-cunha@ec-lyon.fr**

[2] Compredict GmbH,
Darmstadt, 64283, Germany

[3] Univ. Gustave Eiffel, Inria, COSYS/SII, I4S team,
Rennes, 35042, France

[4] Ecole Centrale Lyon, Institut Camille Jordan,
Ecully, 69130, France

Abstract

Lately, there has been a growing interest in applying Machine Learning and Digital Twins for the speed-up of acoustic simulations. However, the lack of interpretability and physics foundation inhibit the widespread usage of these black-box models by the scientific community. In this article, global sensitivity analysis and feature engineering techniques are leveraged to improve the interpretability and physical consistency of ML-based simulations of the Sound Transmission Loss problem for a variety of plate materials. Computationally efficient sensitivity analysis is obtained via the Mean Decrease in Impurity, which is the byproduct of the training of the Random Forest surrogate models. The resulting sensitivity indices were shown to be similar to the traditional Sobol indices and more accurate than Fourier amplitude sensitivity testing for small datasets. Moreover, introducing basic expert knowledge into the ML inputs helped reduce the surrogate prediction error and interpret the physical meaning of sensitivity indices throughout the frequency spectrum.

1 Introduction

Recently Machine Learning (ML) and Digital Twins have enhanced vibroacoustic analyses, being able to, e.g., detect, diagnose and predict system failures with high accuracy [1] and speed up costly simulations [2]. These methods, however, are classified as "black-box", meaning that the causal relationship between the model's inputs and outputs is not explicitly determined. As understanding the underlying physics of the model is crucial in product design to support decision-making and to advance innovation, the adoption of ML in vibroacoustics has been lagging.

One of the most used techniques to improve the interpretability of a model or phenomenon is Sensitivity Analysis (SA). SA methods evaluate the importance of each input parameter to determine the output variability of a system [3]. In the local sensitivity analysis, commonly used in the vibroacoustic domain [4–6], the inputs are varied individually around a given point in the design space to assess their effects on the model output. On the other hand, Global Sensitivity Analysis (GSA) methods, such as Fourier amplitude sensitivity test (FAST) [7] and Sobol's method [8], provide sensitivities indices valid for a broad input variation range. Moreover, GSA can capture input interaction effects and nonlinearities when higher-order sensitivity terms are considered [3]. The drawback of GSA is that it usually demands a specific sampling method and numerous evaluations [9]. Complex vibroacoustic phenomena have been investigated with GSA, e.g.,

the importance of micro-perforated panel absorbers parameters on sound absorption levels [10], the effects of several vehicle components on its interior noise [11], and the sensitivity of Sound Transmission Loss evaluated with analytical methods [12] and with Statistical Energy Analysis [13].

SA has also been employed on ML-based methods to render more meaningful and explainable models [14, 15]. Apart from classic SA methods, the so-called permutation feature importance or Mean Decrease in Accuracy (MDA) [16] can also be applied to any ML model to assess its global first-order sensitivities. In MDA, each feature's importance is evaluated as the drop in the model accuracy given by randomly permuting the feature values, i.e., defining it as a noise input. Chai et al. [17] explored the convenience of evaluating the MDA method at the out-of-bag samples of an RF and applied it to the STL problem of a honeycomb sandwich plate. Besides that, some algorithms have sensitivity indices as a post-processing step of the training, as in polynomial chaos expansions (PCE) [18], gaussian process regressors [19] and decision tree-based methods [20]. The Mean Decrease in Impurity (MDI) is an example of a sensitivity method that comes as a by-product of Random Forest (RF) and which sensitivity indices are similar to the Sobol's total sensitivity indices, being more flexible to implement [21].

Recent research also integrates physical knowledge into the ML model to increase its accuracy and interpretability for applications in diverse scientific fields. Willard [22] surveyed the methods applied with this purpose including, e.g., penalizing physical inconsistencies during the ML training and defining ML architectures that encode the symmetries and variables dependencies of the physical problem. A straightforward method to embed domain expertise in the ML is to include physics-guided features through feature engineering, as recently applied in thermal [23], fluid flows [24], and material science problems [25].

This study aims to apply physics-guided features and the MDI global sensitivity analysis to develop an interpretable and explainable RF-based surrogate model for the classical vibroacoustic problem of STL with no additional computational cost. The present paper extends the work in [26] by performing a comparison of MDI indices with Sobol and FAST indices regarding their formulation, accuracy, and time elapsed, and by encompassing different incident fields and material properties, namely isotropic, orthotropic, and sandwich materials. The performance and the results obtained are compared with the STL sensitivity analyses in [12, 17]. The methodology presented is extendable to other engineering problems and experimental setups, where it may enhance system identification and scientific discoveries.

The paper is organized as follows. Section 2 briefly presents the theory of the classical Sobol's and FAST methods. Section 3 introduces RF and MDI concepts and formulation. Section 4 shows the analytical formulations for the STL for the different plate materials analyzed. The results of the comparison between Sobol, FAST, and MDI are presented in Section 5. The MDI-based sensitivity results in Section 6 bring light to different aspects of the coincidence phenomenon in the STL problem. The influence of including physics-guided features on the surrogate accuracy and the total sensitivity indices are presented in Section 7. Dimension reduction has also been applied following GSA. Section 8 contains the conclusions.

2 Variance based sensitivity analysis

In the variance-based sensitivity analysis, the importance of each input and input interaction is assessed by their contribution to the output variance. The Sobol's decomposition of variance states that the total variance of the output of a model $Y = f(\mathbf{x}) = f(x_1, x_2, \ldots, x_D)$ can be represented as the sum of the individual effects of the each input x_i, denoted as V_i, and the higher-order effects from the interactions between a set of inputs as long as some conditions are met [8, 27]. That is:

$$Var[Y] = V = \sum_{i=1}^{D} V_i + \sum_{i=1}^{D} \sum_{j>i}^{D} V_{ij} + \cdots + V_{1,2,\ldots,D}. \tag{1}$$

Following [8, 27], the first-order Sobol sensitivity indices or main effect indices of the input variable x_i can

be expressed in terms of conditional expected values as

$$S_i = \frac{V_i}{V} = \frac{E_{\mathbf{x}_{\sim i}}\left(Y \mid x_i\right)}{V},$$ (2)

where $\mathbf{x}_{\sim i}$ denotes the set of all variables but x_i and the numerator of S_i is equivalent to the expected average reduction of the output variance when x_i is fixed [28]. The total contribution of the variable x_i to the variance output, including the effects caused by its interactions with other variables, is measured by the total sensitivity index [3]:

$$S_{T_i} = 1 - \frac{Var_{\mathbf{x}_{\sim i}}(E_{x_i}(Y|\mathbf{x}_{\sim i}))}{V}.$$ (3)

The total sensitivity indices can be interpreted as the remaining variance when all terms but x_i are fixed [29]. The sum of the total sensitivity indices is equal to or greater than one. When equals to one, the function is additive, i.e., only the first-order terms contribute to the variance, and there is no effect of the interaction between any parameter, what read as $S_{T_i} = S_i$.

Evaluating variance-based sensitivity indices involves sampling and uncertainty quantification stages usually based on Monte Carlo or quasi-Monte Carlo integral methods, which are computationally intensive. A popular and less costly technique to evaluate variance-based sensitivity indices is the Fourier amplitude sensitivity test (FAST), developed in 1973 by Cukier et al. [7] to evaluate the main effect indices. The FAST method was extended by Saltelli et al. [30] to include the computation of the total effects and is now integrated with Sobol's indices. FAST uses a particular period sampling approach to define the multiple Fourier series expansion that approximates the function $f(\mathbf{x})$. As the Fourier series expansion can be decomposed as an Analysis Of Variance (ANOVA)-like decomposition, the components of the model variance can be modeled in terms of the Fourier coefficients [29]. The FAST and Sobol methods assume uncorrelated and independent variables, otherwise, they lead to biased results if specific methodologies for correlated and dependent variables are not applied [15].

3   Random forest surrogates and mean decrease in impurity SA

Surrogate models or metamodels are approximations of costly functions that are constructed based on inferred information from a set of input-output pairs $(\mathbf{q}, \mathbf{y})$ sampled with the true function. An increasingly popular way to construct these surrogates is to use ML regressors to make the data inference. Most ML models are constructed based on a structure/representation that defines the relation between inputs and outputs depending on its parameters. These parameters are optimized during the ML training to minimize the cost function, which defines the error between the predicted ML output and the true output.

Many ML methods use decision trees as its basic structure to define the data relations. The decision tree splits the input feature space using simple rules at each of its branches [16]. Each split at a node n is defined by a threshold t_n applied to an input feature q_{i_n} and divides the space at the current branch $\mathcal{C}$ into two new subspaces (two new branches):

$$\mathcal{C}^-(q_{i_n}, t_n) = \{(\mathbf{q}, \mathbf{y}) \in \mathcal{C} : q_{i_n} \leq t_n\},$$
$$\mathcal{C}^+(q_{i_n}, t_n) = \{(\mathbf{q}, \mathbf{y}) \in \mathcal{C} : q_{i_n} > t_n\}.$$

Each node split aims to aggregate samples with similar outputs. Therefore, during the training process the pair (q_{i_n}, t_n) that minimizes the splitting error at node n, also called impurity criterion $G_n(q_{i_n}, t_n)$, is chosen to split the domain. A common impurity criterion used in regression problems is based on the Mean Squared Error (MSE) of each subspace, defined as

$$G_n(q_{i_n}, t_n) = \frac{L^-}{L} \left(\frac{1}{L^-} \sum_{y \in \mathcal{C}^-} (y - \mu^-)^2 \right) + \frac{L^+}{L} \left(\frac{1}{L^+} \sum_{y \in \mathcal{C}^+} (y - \mu^+)^2 \right),$$ (4)

where μ^- and μ^+ denote the mean output value of the subspaces $\mathcal{C}^-$ and $\mathcal{C}^+$, respectively, and L, L^- and L^+ are the number of samples in subspaces $\mathcal{C}$, $\mathcal{C}^-$ and $\mathcal{C}^+$.

The binary divisions of the decision tree continue successively until an established criterion is met, e.g., the decision tree reaches its maximum depth. At the terminal nodes, a scalar is assigned as output prediction for each final subspace. Individual decision trees can be combined in an ensemble model using bagging to create a Random Forest (RF) predictor [16]. The bagging procedure randomly selects distinct sub-datasets to train each tree, ensuring different trees. The final RF prediction is the average of the decision tree predictions in the forest and, therefore, it has lower variance and generalizes better than individual predictors.

Besides being efficient and able to approximate complex models, RFs are notable for being interpretable ML models. They provide different ways to access feature importances that relate to sensitivity indices. One of them is the Mean Decrease in Impurity (MDI), a by-product of the RF training. The principle of MDI is that the contribution of each input feature to reduce the impurity error is a measure of its importance. Given an RF with Φ_κ trees, $\kappa = 1, \ldots, T$, the MDI importance can be defined as [16,20]:

$$\text{MDI}(q_i) = \frac{1}{T} \sum_{\kappa=1}^{T} \sum_{n \in \Phi_\kappa} 1(q_{i_n} = q_i) \frac{L}{L_{tot}} \Delta G_n(q_{i_n}, t_n), \tag{5}$$

where $1(q_{i_n} = q_i)$ is one if $q_{i_n} = q_i$ and zero otherwise. The term $\Delta G_n(q_{i_n}, t_n)$ denotes the changes in impurity at node $n \in \Phi_\kappa$ and it is weighted by the fraction of samples at that node $\frac{L}{L_{tot}}$. Therefore, similarly to how the total Sobol indices can be interpreted as the effect of one input variable in the output variance decrease, the MDI indices are the effect of the input feature in the RF impurity decrease. Indeed, Scornet [31] proved that, for the case of additive functions with independent variables, the MDI of a decision tree provides a decomposition of the output variance. In the presence of interactions, consistent MDI can be obtained via RF, i.e., by averaging the MDI of several decision trees [31]. Scornet also showed that the MDI is biased towards positively correlated variables.

MDA is also often applied to evaluate the SA of RF models. Jaxa-Rozen and Kwakkel [21] compared MDI and MDA indices with Sobol and Moris metrics for different study cases and highlighted that both MDI and MDA meet the criteria of an *"ideal"* sensitivity metric, i.e., *"suitable for global sampling projects, independent of model structure, relatively easy to implement numerically, stable across all sample sizes and bootstrap resamples and applicable with generic input sampling and heterogeneous input types"*. Nonetheless, MDI and MDA do not provide the direct effects of inputs on output variance, but their relative importances. The direct effects can be assessed by applying traditional SA approaches to the fitted RF-based surrogate.

4   Analytical sound transmission loss

The sound insulation capacity is an important characteristic of a structure, which is deeply studied in acoustic projects. The assessment of the sound insulation capacity is usually done by the sound transmission loss (STL) analyses, which evaluate the relation between the sound power reaching the structure I_I and the sound power transmitted through the structure I_T. Following [32, 33], the STL of a plane wave is evaluated by

$$STL = -log_{10}\tau(\phi, \theta, \omega) = -log_{10}\left(\frac{I_T}{I_I}\right) = -log_{10}\left|\frac{\mathbf{P_T}}{\mathbf{P_I}}\right|^2, \tag{6}$$

where τ is the acoustic transparency of a harmonic plane wave of frequency ω, azimuth angle ϕ and incident angle θ, and P_I and P_T are the incident and transmitted sound fields, respectively.

The sound pressure field can be generically defined as

$$\mathbf{P}_* = p_* e^{i(\omega t - k_x \mathbf{x} - k_y \mathbf{y} \pm k_z \mathbf{z})}. \tag{7}$$

Here, $\mathbf{P}_*$ can refer to either the incident, transmitted, or reflected sound pressure field, and p_* is the associated pressure amplitude. The components of the wave number are defined as $\mathbf{k} = \begin{pmatrix} k_x & k_y & k_z \end{pmatrix}^T =$

$\frac{\omega}{c_0}\left(\sin\theta\cos\phi \quad \sin\theta sin\phi \quad \cos\theta\right)^T$, where c_0 is the sound speed through the fluid. Both the incident and the transmitted sound pressure $\mathbf{P_I}$ and $\mathbf{P_T}$ have a z component in the positive direction according to the convention in Figure 1, while the sound field reflected by the plate $\mathbf{P_R}$ has a negative component in z. Hereinafter, the term $e^{i(\omega t - k_x \mathbf{x} - k_y \mathbf{y})}$ will be omitted by convenience.

The continuity between the speed of the fluid and the plate at the interface can be stated as

$$\begin{cases} ik_z(p_R - p_I) = \rho_0\omega^2 w, & \text{for } z = 0 \text{ at the incident side,} \\ ik_z p_T = -\rho_0\omega^2 w, & \text{for } z = 0 \text{ at the transmission side,} \end{cases} \tag{8}$$

where ρ_0 is the fluid density and w the plate displacement. From Eq. 8, it is deduced that $p_R = p_I - p_T$, and, therefore, the fluid pressure force acting in the plate is given by $F = (p_I + p_R) - p_T = 2(p_I - p_T)$.

The plate constitutive equation can be formulated as a function of the plate impedance Z as

$$iZ\omega w = F = 2(p_I - p_T). \tag{9}$$

Combining Eq. 8 and Eq. 9, the ratio between incident and transmitted pressures is given by

$$\frac{p_I}{p_T} = \left(1 + \frac{Z\cos(\theta)}{2\rho_0 c_0}\right). \tag{10}$$

This ratio can be used to calculate the acoustic transparency of a plane wave τ and the STL for τ (Eq. 6). Moreover, the acoustic transparency for a diffuse field $\tau_d(\omega)$ is the weighted average transmission coefficient over all possible angles $\theta \in [0, \pi/2]$ and $\phi \in [0, 2\pi]$:

$$\tau_d(\omega) = \frac{\int_0^{2\pi}\int_0^{\pi/2} \tau(\phi,\theta,\omega)\cos\theta\sin\theta\,d\theta d\phi}{\int_0^{2\pi}\int_0^{\pi/2}\cos\theta\sin\theta\,d\theta d\phi}. \tag{11}$$

The sound transmission reaches its maximum value whenever the wavelength of the acoustic wave projected onto the plate, also called the trace wavelength, coincides with the wavelength of the natural propagating waves of the plate, which is known as the coincidence phenomenon. Thus, the coincidence frequency ω_{coin} is the frequency with which the projected acoustic wavenumber $k_t = \frac{\omega}{c_0}\sin\theta$ is equal to the plate natural propagating wavenumber $k_p(\omega)$. In the case of diffuse fields, the minimum frequency at which coincidence takes place (i.e., when $\sin\theta = 1$) is called critical frequency ω_{crit}.

4.1 Isotropic model

The structural impedance of a Kirchhoff-Love isotropic plate with thickness h, density ρ, Young's modulus E, Poisson ratio v, structural damping η and plate bending stiffness $D = \frac{Eh^3}{12(1-v^2)}(1 + i\eta)$ impinged by an acoustic plane wave is given by

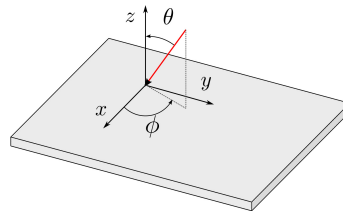$$Z(\omega,\theta) = \left(1 - \omega^2\frac{D}{\rho h c_0^4}\sin^4\theta\right)i\omega\rho h. \tag{12}$$

Figure 1: MDI indices for the STL analysis of isotropic plates for a plane wave with $\theta = 60°$.

By replacing the impedance expression in Eq. 10 with Eq. 12, one can evaluate the acoustic transparency and the STL for the isotropic plate. As observed in [32], while the first term of $Z(\omega, \theta)$ in Eq. 12 is dominated by the plate inertia, the second term is stiffness-controlled. This characteristic of isotropic plates is later observed in this paper in STL curves.

The natural propagating wavenumber of the thin isotropic plate is the bending wavenumber $k_p = \frac{\omega^2 \rho h}{D}^{1/4}$ [32]. Therefore, its coincidence frequency occurs at

$$\omega_{coin}(\theta) = \frac{c_0^2}{\sin^2 \theta} \sqrt{\frac{\rho h}{D}}. \tag{13}$$

4.2 Orthotropic plates

Following [12], the structural impedance of an infinite orthotropic plate in the STL problem is given by

$$Z(\omega, \theta, \phi) = \left(1 - \omega^2 \frac{D(\phi)}{\rho h c_0^4} \sin^4 \theta\right) i\omega\rho h, \tag{14}$$

where $D(\phi)$ is the heading bending stiffness of the plate and is defined as

$$\begin{aligned} D(\phi) &= D_x \cos^4 \phi + 2D_{xy} \sin^2 \phi \cos^2 \phi + D_y \sin^4 \phi \\ &= \left(E_x \cos^4 \phi + 2(E_y v_{xy} + 2G_{xy}) \sin^2 \phi \cos^2 \phi + E_y \sin^4 \phi\right) \frac{h^3(1 + i\eta)}{12\left(1 - \frac{E_y}{E_x} v_{xy}^2\right)}. \end{aligned} \tag{15}$$

In Eq. 15 the sub-indices correspond to the direction relative to each material property, and G_{xy} is the in-plane shear modulus.

The behavior of the plate bending wave on an orthotropic plate varies according to the wave's direction. Thus, the coincidence frequency occurs at different azimuth angle ϕ, and is given by

$$\omega_{coin}(\phi, \theta) = \frac{c_0^2}{\sin^2 \theta} \sqrt{\frac{\rho h}{D(\phi)}}. \tag{16}$$

Two special cases of Eq. 16 are important in the STL analysis of orthotropic plates, namely the critical frequencies corresponding to the directions x and y, i.e. when $\phi = 0°$ and $\phi = 90°$, respectively, and are calculated as

$$\omega_{crit,x} = c_0^2 \sqrt{\frac{\rho h}{D_x}} \quad \text{and} \quad \omega_{crit,y} = c_0^2 \sqrt{\frac{\rho h}{D_y}}. \tag{17}$$

4.3 Sandwich panels

Sandwich structures are composite structures composed of two thin and stiff plates, the skin layers, interspersed with a thick layer of lightweight material, the core layer, and are widely used due to their good stiffness-weight ratio. Sandwich material can be designed to shift the critical frequency to higher frequencies and increase the transmission loss at coincidence due to the dampening effects of the core layer. Narayanan and Shanbhag [34] proposed an analytical implementation of the STL for infinite damped sandwich panels, considering that the deformations of the skin and core can be modeled respectively as purely bending and shear deformations and that the skin material is non-dissipative.

According to [34], the structural impedance of the infinite sandwich panels approximates as

$$Z(\omega, \theta) = \frac{k_t^6 D_s g\beta Y}{\omega(k_t^2 + g)^2 + g^2\beta^2} + i\left(\omega m - \frac{D_s k_t^4}{\omega} \frac{1 + gY(k_t^2 + g + g\beta^2)}{(k_t^2 + g)^2 + g^2\beta^2}\right), \tag{18}$$

where β is the core loss factor, $Y = 3(1 + h_c/h_s)^2$ is the geometric parameter, m is the mass density of the entire structure, D_s is the skin bending stiffness, $g = \frac{2G_c(1-v_s^2)}{E_s h_s h_c}$ is the shear parameter of the core and G_c is the shear modulus of the core. The subindices c and s relate respectively to core and skin. The coincidence frequency equation for the sandwich panels can be found in [34].

5   Comparison of variance-based and MDI sensitivity analyses

In this section, the total importances obtained with the variance-based SA using Sobol and FAST are compared with the MDI results regarding accuracy and computing time. All analyses were carried out on a desktop with a hexa-core 3.1 GHz processor and 32 GB of RAM using *Python* as the primary programming language and *Matlab* functions to solve the analytical STL. The *Salib* library [35] was used to obtain the sensitivity indices with Sobol and FAST approaches, while the RF models were instantiated and trained using *sklearn*. One RF with 100 trees is trained for each of the N_ω outputs and 15% of the database is used to assess the RFs accuracy. The same desktop and RF architecture is used in the remaining sections of this paper. The following comparison was made for the STL of isotropic infinite plates impinged by a diffuse field. The five-dimensional design space considered is presented in Table 1 and encloses a broad range of material properties, including the aluminum grades.

Table 1: Design space considered for the isotropic plate analyses.

Inputs	h	E	ν	ρ	η
Units	mm	GPa	-	kg/m^3	$\%$
Lower Bound	7	55	0.20	2300	0.1
Upper Bound	8	85	0.35	3300	1

The MDI indices are comparable with the variance-based total effect indices S_T but on different scales, as the MDI indices sum up to one, while $\sum_i S_{T_i} >= 1$. Thus, to enable a prompt comparison between MDI indices and S_T, the importances will be scaled as $\bar{S}_{T_i} = \frac{S_{T_i}}{\sum_i S_{T_i}}$. MDI and FAST accuracies were evaluated having as a reference model R the Sobol analyses with 24576 evaluations, which was determined after a convergence test. The accuracy error of the sensitivity indices from analysis A in relation to the reference R is evaluated by

$$\varepsilon(A, R) = \frac{1}{N_\omega D} \sum_\omega^{N_\omega} \sum_i^D |\bar{S}_{T_i}^A - \bar{S}_{T_i}^R|. \tag{19}$$

Figure 2 shows the comparison between the performance of FAST and RF. The MDI indices are more accurate with few evaluations, while the FAST method is slightly more accurate for large databases. The elapsed time for the same number of samples is similar for both methods since sampling is the most time-consuming stage of both approaches. Recently Chai et al. [17] showed good agreement between FAST and MDA importances obtained with RF-based surrogates for an STL analysis, however, the approach did not prove to be advantageous due to the extra cost of MDA and its lack of mathematical foundation.

The scaled total sensitivity importances calculated with the three approaches are shown in Figure 3 for visual comparison. Both MDI and FAST importances were computed using 1280 evaluations, being that the root mean squared error (RMSE) of the surrogate evaluated in the test dataset was 0.40 dB. Figure 2a and Figure 3 indicate that there is a good agreement among the sensitivity indices calculated by all approaches and that the MDI indices obtained with RF-based surrogates are suitable indicators of input importances when few samples are available.

Besides that, the MDI presents other advantages. First, the RF can be trained based on a generic sampling strategy, while FAST requires a particular sampling scheme and can not reuse previous evaluations of the model. Furthermore, once the RF-based surrogate is trained, it can be used to perform a multitude of forwarding analyses in a fraction of the time, being suitable for uncertainty propagation, optimizations, and
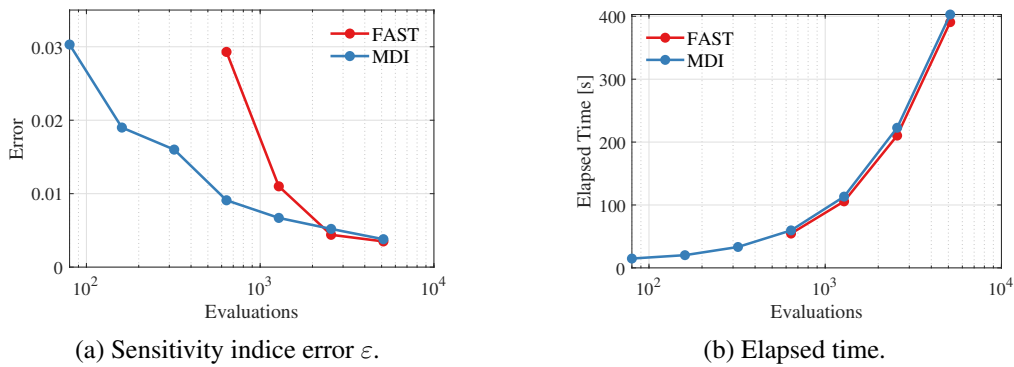
(a) Sensitivity indice error ε.

(b) Elapsed time.

Figure 2: Comparison of Sensitivity Analyses approaches.

(a) Sobol total sensitivity indices.

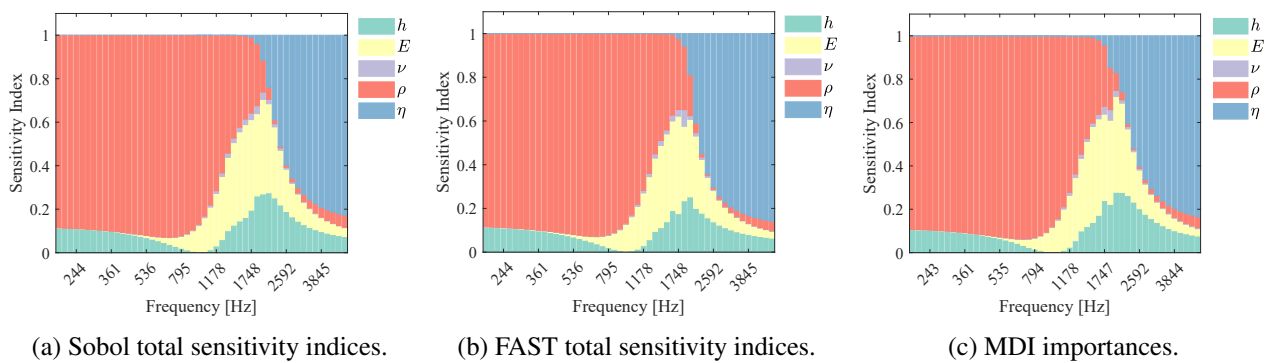(b) FAST total sensitivity indices.

(c) MDI importances.

Figure 3: Total sensitivity indexes of the STL analyses for isotropic plates.

classical sensitivity analysis. Figure 4 illustrates an example in which the RF-based surrogate was used to replace the true STL model in the calculation of Sobol's first order indices with 24576 evaluations. While the elapsed time using the true model was $1867s$, the analysis using the surrogate took $23s$, that is, more than 80 times faster. At a previous stage, the sampling and training of this surrogate took more $111s$. The higher-order sensitivity indices can be readily obtained similarly.

(a) True STL model is used to evaluate the outputs.

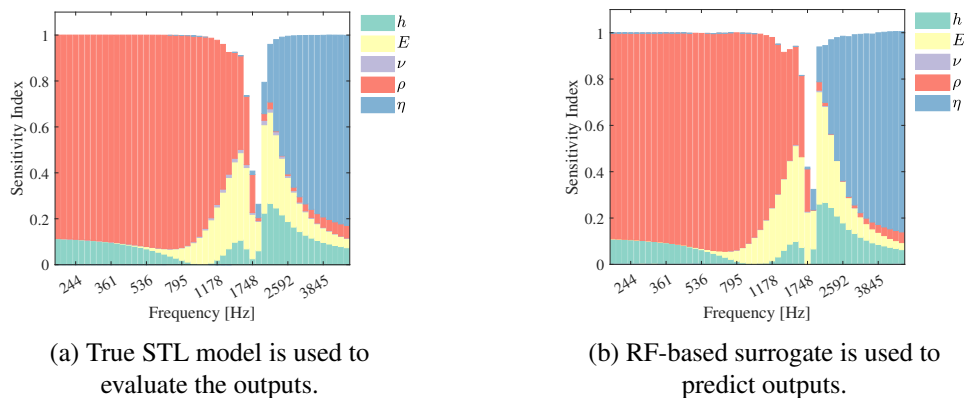(b) RF-based surrogate is used to predict outputs.

Figure 4: First-order sensitivity indices with Sobol algorithm.

6 MDI Results for isotropic, orthotropic and sandwich plates

MDI analysis can be used to approximate expensive GSA analysis but also to bring interpretability to the surrogate model, a constant demand from the scientific community regarding black-boxes. This section analyzes the STL for different materials and incident acoustic fields through the use of surrogate models and

the MDI sensitivity analysis. It should be noted that the MDI results depend on the selected design space, as is the case for every GSA, thus, the results cannot be generalized to other input ranges. In this work, design spaces with a broad variation range were selected to train surrogates suitable for design exploration.

6.1 Isotropic plates

The same design space and database from Section 5 is used in this Section. According to the theory of STL for infinite isotropic plates [32], it is known that two regions are expected: the inertia controlled region, in which the STL can be approximated by the mass law, and the stiffness controlled region. These regions correspond to the region where the first and second terms of the structural impedance of the plate in Eq. 12 predominate, respectively.

The MDI sensitivity analysis performed for a plane wave with $\theta = 60°$ (Figure 5) clearly shows both regions, the inertia controlled, where the variance in ρ and h defines all the output variance and goes up to around 2000 Hz, and the stiffness controlled region where E and h play major roles. The transition frequency range between these regions matches the range of the coincidence frequency for this space design, which ranges from approximately 1680 Hz to 2680 Hz. According to STL physics, the amplitude of the STL valley at the coincidence frequency is controlled by the plate damping η, which importance slightly rises at this frequency range in Figure 5.
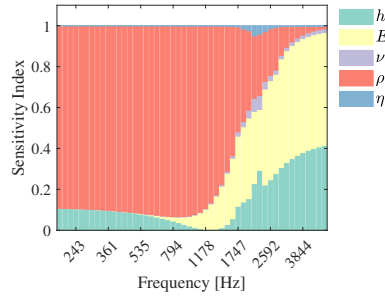

Figure 5: MDI indices of isotropic plates STL for a plane wave with $\theta = 60°$. Surrogate RMSE: 0.97 dB.

In the case of an incident diffuse field (Figure 3), the coincidence phenomenon occurs at the frequencies above the critical frequency, which varies approximately between 1260 and 2000 Hz. It is observed that in this frequency range, the importance of the inputs E and h, related to the stiffness, predominates, while the damping effect is predominant for higher frequencies. This behavior was also remarked in [12], which concluded that for plane waves the location of the STL dip has a greater effect on the output variance than its amplitude, explaining why the damping importance near the coincidence is smaller than expected. For the diffuse field analysis, the dip location is important at the critical frequency range, but the STL amplitude is more important in the coincidence region, where damping predominates. These results are summarized in Table 2 and corroborate that the RF-based surrogate is physically consistent and interpretable.

Table 2: Main MDI importances at different regions of STL of isotropic plates.

	$\omega < \omega_{crit}$	At $\omega \approx \omega_{crit}$	$\omega > \omega_{crit}$
Plane Wave	ρ, h	$\rho, h, E + \eta$ peak	E, h
Diffuse Field	ρ, h	E, h	η

6.2 Orthotropic plates

The investigations of the STL for an orthotropic plate were performed considering a unidirectional fiber-reinforced composite plate in which carbon fibers are oriented along the x axis with resin as matrix material,

resulting in different Young Modulus in the in-plane directions. The material properties ranges are presented in Table 3, from where 1792 points were sampled for each analysis. The complexity of the STL analysis increases for the orthotropic plates as it has two more dimensions than isotropic plates and the coincidence phenomena occur in multiple directions.

Table 3: Design space considered for the orthotropic plate analyses.

Inputs	h	E_x	ν	ρ	η	E_y	G_{xy}
Units	mm	GPa	-	kg/m^3	$\%$	GPa	GPa
Lower Bound	3.25	190	0.25	1300	0.1	5	50
Upper Bound	4	260	0.35	1800	1	10	65

The incident plane waves cases were all evaluated with $\theta = 80°$, close to grazing angle, and with azimuth angle ϕ equals $0°$, $45°$, and $90°$, to evaluate the behavior of the coincidence phenomenon and STL curve for different wave directions. The MDI indices evaluated for STL of each plane wave are depicted in Figures 6a to 6c. It is noted that, regardless of the direction of the incident wave, the low-frequency region is controlled by plate inertia. Nonetheless, the behavior of the MDI indices in the high-frequency region differs for each wave direction.

The results for $\phi = 0°$ are similar with the ones for the isotropic plate (Figure 5), where h and E_x are the most important variables. Besides that, the small peaks of damping and stiffness importances coincide with the range of $\omega_{crit,x}$, which is from approximately 1140 to 1740Hz, according to Eq. 16. Similar peaks are identified for the results with $\phi = 45°$ at higher frequencies, indicating where the coincidence is probably occurring. The in-plane shear modulus G_{xy} has considerable effects when $\phi = 45°$, which is in line with the expected physical behavior for a highly orthotropic material. Finally, for $\phi = 90°$, the bending stiffness in the y direction becomes the most important variable at high frequencies and the coincidence peak also coincides with the $\omega_{crit,y}$ range, which goes from around 5800 to 10660 Hz.

(a) Plane wave with $\theta = 80°$ and $\phi = 0°$. Surrogate RMSE: 0.27 dB.

(b) Plane wave with $\theta = 80°$ and $\phi = 45°$. Surrogate RMSE: 0.40 dB.

(c) Plane wave with $\theta = 80°$ and $\phi = 90°$. Surrogate RMSE: 0.81 dB.

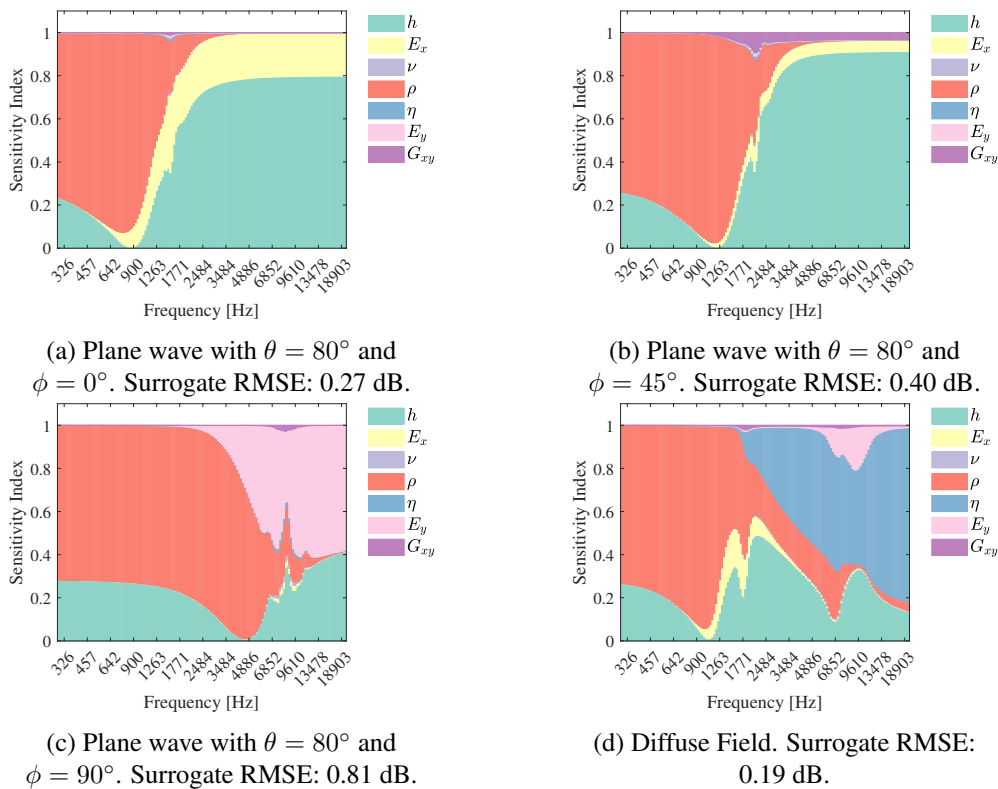(d) Diffuse Field. Surrogate RMSE: 0.19 dB.

Figure 6: MDI indices of the STL analyses of orthotropic plates evaluated with RF-based surrogate.

Figure 6d presents the MDI indices for the diffuse field analyses, where there is a remarkable increase in

E_x and E_y importances in the regions of $\omega_{crit,x}$ and $\omega_{crit,y}$ ranges, respectively. In both regions, h also had increased importance. In the entire coincidence region, the damping importance is primordial. The findings for the MDI indices of the orthotropic plates are summarized in Table 4. In general, for STL with an incident plane wave, the STL at $\omega > \omega_{coinc}$ is controlled by the corresponding stiffness. For STL with the diffuse field, the importance of variables related to stiffness increases at the critical frequencies, while the coincidence region is damping-controlled.

Table 4: Main MDI importances at different regions of STL for orthotropic plates. Results were obtained for plane wave (PW) cases with incident angle $\theta = 80°$ and variable azimuth angle ϕ, and for the diffuse field case.

	$\omega < \omega_{crit,x}$	$\omega \approx \omega_{crit,x}$	$\omega_{crit,x} < \omega < \omega_{crit,y}$	$\omega \approx \omega_{crit,y}$	$\omega > \omega_{crit,y}$
PW: $\phi = 0°$	ρ, h	$\rho, h, E_x + \eta$ peak	E_x, h	E_x, h	E_x, h
PW: $\phi = 45°$	ρ, h	ρ, h	$\rho, h, G_{xy} + \eta$ peak	E_x, G_{xy}, h	E_x, G_{xy}, h
PW: $\phi = 90°$	ρ, h	ρ, h	ρ, h	$\rho, h, E_y + \eta$ peak	E_y, h
Diffuse Field	ρ, h	E_x, h	η	G_{xy}, η	η

6.3 Sandwich panels

The RF-based surrogates for sandwich plates were trained with 4096 evaluations from the design space in Table 5 considering eight material parameters. The MDI indices were evaluated for the STL with an incident plane wave with $\theta = 80°$, Figure 7a, and STL with a diffuse field, Figure 7b.

Table 5: Design space considered for the sandwich plate analyses.

Inputs	h_s	E_s	ν_s	ρ_s	β	h_c	G_c	ρ_c
Units	mm	GPa	-	kg/m^3	$\%$	mm	GPa	kg/m^3
Lower Bound	1.5	55	0.20	2300	0.1	25	15	200
Upper Bound	2	85	0.35	3300	1	35	25	300

The MDI results for a sandwich plate show that the core shear modulus also has considerable importance at low frequencies, different from the materials from previous sections in which only inertia controlled the low-frequency region. According to the coincidence frequency equation presented by [34], the expected range would be from around 4900 to 11400 Hz, which coincides with the peak in β at Figure 7a. For higher frequencies, the STL is controlled by thickness and Young Modulus, variables that compose the skin bending stiffness. Similar observations can be made for the results at low frequency with a diffuse field, while above the critical frequency the sandwich plate STL with a diffuse field is controlled by β, as shown in Figure 7b.

7 Physics-guided features leveraged by surrogates

Previous knowledge of the physics of the problem can be built into surrogate models through the addition of physics-guided features by simply adding pre-processing steps that rearrange the system variables in terms of physical meaning. This section evaluates the impact of adding these physics-guided features on the accuracy of the surrogate and on the sensitivity indices. The analyses were carried out for isotropic, orthotropic, and sandwich plates with an incident diffuse field. It is worth mentioning that the RFs are retrained with the same databases used in previous sections, therefore, the time elapsed to perform the following analyses is negligible. To keep only the most relevant features, the features with an average importance of less than 2.5% were excluded from the analyses.

Table 6 shows the physics-guided features added for each analysis and underlines the selected relevant features. While the parametric study in [34] concluded that the core shear parameter g was the most influential

(a) Plane wave with $\theta = 80°$. Surrogate RMSE: 1.89 dB.

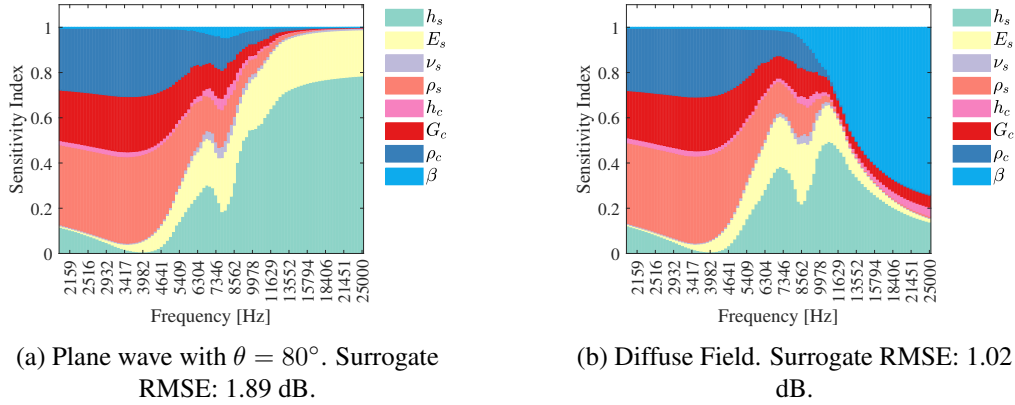(b) Diffuse Field. Surrogate RMSE: 1.02 dB.

Figure 7: MDI indices of the STL analyses of sandwich plates evaluated with RF-based surrogate.

parameter for the STL of a sandwich plate, the current analysis indicates that the importance of g is negligible. This can be explained as here the output variance is better explained by other terms correlated to g than by g itself.

Table 6: Physics-guided features included and important variables selected underlined.

	STL Variables	Physics-guided features
Isotropic Plates	$h, \underline{E}, \nu, \underline{\rho}, \underline{\eta}$	$\underline{m}, \underline{D}$
Orthotropic Plates	$h, E_x, E_y, G_{xy}, \nu, \rho, \eta$	$\underline{m}, \underline{D_x}, \underline{D_y}, D_{xy}$
Sandwich Plates	$h_s, E_s, \nu_s, \underline{\rho_s}, h_c, \underline{G_c}, \underline{\rho_c}, \underline{\beta}$	$\underline{m}, \underline{D_s}, g, Y$

Figure 8 shows the MDI indices for the plate materials considered. Three general aspects are noted:

- In the mass-controlled region the variance is entirely defined by m, except for the sandwich plate results where G_c also has a significant contribution.

- The regions of critical frequencies are preceded by an increase in the importance of densities with a subsequent increase in the importance of the stiffness that controls the vibration mode respective to the coincidence taking place.

- In the coincidence regions and STL variability is composed mainly of the effects of damping.

(a) Isotropic Plate.

(b) Orthotropic Plate.
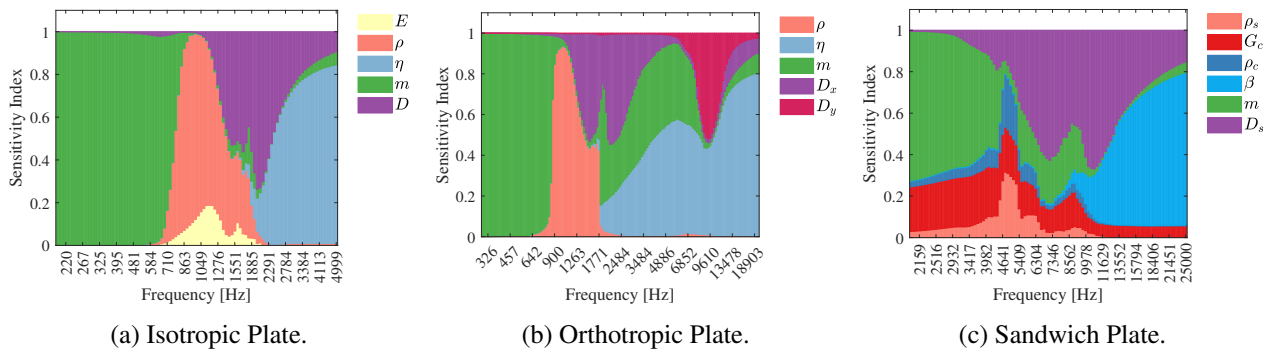
(c) Sandwich Plate.

Figure 8: MDI indices of STL analyses with addition of physics-guided features and carrying out features selection.

The results show that the variable effects can be better represented within the added physical-guided terms. For example, the original analysis of the isotropic case (Figure 3c) showed a contribution of h both at low and high frequencies, while in Figure 8a these contributions are encompassed by m and D at low and high frequencies, respectively. However, it should be stressed that the physics-guided features depend on or

Table 7: Accuracy of the RF-based surrogate with and without physics-guided features (PGF) in terms of the RMSE.

	Accuracy without PGF	Accuracy with PGF
Isotropic Plates	0.40 dB	0.22 dB
Orthotropic Plates	0.19 dB	0.16 dB
Sandwich Plates	1.02 dB	0.71 dB

correlate with other input variables and the MDI indices may be biased towards them [31]. Therefore, the MDI indices of Figure 8a can be helpful in identifying the contributions of complex physical terms in the system output, but they should not quantitatively determine their importance. In addition to assisting the interpretation of MDI analysis results, the addition of the engineered features guides the RF model to follow the known physics. In this way, the physics-guided features increase the physical consistency of the black box and improve its accuracy, as seen in Table 7.

8 Conclusion

Interpretable and physics-guided RF-based surrogate models were implemented for the STL analysis through MDI sensitivity analyses and feature engineering. The STL problems were analytically modeled for infinite plates with isotropic, orthotropic, and sandwich materials, considering plane wave and diffuse field as incident acoustic fields.

The MDI-based sensitivity indices showed good accuracy related to the reference Sobol's total sensitivity indices even for a small number of function evaluations. The MDI method proves to be potentially advantageous over FAST since it does not depend on a minimum number of evaluation points and specific sampling methods, furthermore, its performance was superior to or close to FAST performance for the same number of evaluations. However, it should be highlighted that the MDI accuracy depends on the RF's accuracy. The inclusion of physics-guided features was beneficial for surrogate accuracy. Furthermore, the combined use of MDI with feature engineering allows exploring the importance of user-defined terms, clarifying the physical relationships of the analyses.

These capabilities were illustrated for the STL analyses performed, which elucidated different aspects of the STL, enriching the discussions in [12, 17, 26]. Therefore, physics-based interpretations enabled by the methods implemented can increase the level of confidence in the surrogate and allow an in-depth comprehension of the physical phenomena with the potential to boost scientific discovery supported by data.

Acknowledgements

References

[1] M. Stender, M. Tiedemann, D. Spieler, D. Schoepflin, N. Hoffmann, and S. Oberst, "Deep learning for brake squeal: Brake noise detection, characterization and prediction," *Mechanical Systems and Signal Processing*, vol. 149, p. 107181, 2021.

[2] I. Ibrahim, R. Silva, M. Mohammadi, V. Ghorbanian, and D. A. Lowther, "Surrogate-based acoustic noise prediction of electric motors," *IEEE Transactions on Magnetics*, vol. 56, no. 2, pp. 1–4, 2020.

[3] T. Homma and A. Saltelli, "Importance measures in global sensitivity analysis of nonlinear models," *Reliability Engineering & System Safety*, vol. 52, no. 1, pp. 1–17, 1996.

[4] J. Zhang, X. Xiao, X. Sheng, C. Zhang, R. Wang, and X. Jin, "Sea and contribution analysis for interior noise of a high speed train," *Applied Acoustics*, vol. 112, pp. 158–170, 2016.

[5] N. H. Kim and J. Dong, "Shape sensitivity analysis of sequential structural–acoustic problems using fem and bem," *Journal of sound and vibration*, vol. 290, no. 1-2, pp. 192–208, 2006.

[6] F. Scarpa, "Parametric sensitivity analysis of coupled acoustic-structural systems," *J. Vib. Acoust.*, vol. 122, no. 2, pp. 109–115, 2000.

[7] R. Cukier, C. Fortuin, K. E. Shuler, A. Petschek, and J. H. Schaibly, "Study of the sensitivity of coupled reaction systems to uncertainties in rate coefficients. i theory," *The Journal of chemical physics*, vol. 59, no. 8, pp. 3873–3878, 1973.

[8] I. M. Sobol', "On sensitivity estimation for nonlinear mathematical models," *Matematicheskoe modelirovanie*, vol. 2, no. 1, pp. 112–118, 1990.

[9] F. Sarrazin, F. Pianosi, and T. Wagener, "Global sensitivity analysis of environmental models: Convergence and validation," *Environmental Modelling & Software*, vol. 79, pp. 135–152, 2016.

[10] Z. Laly, N. Atalla, S.-A. Meslioui, and K. El Bikri, "Sensitivity analysis of micro-perforated panel absorber models at high sound pressure levels," *Applied Acoustics*, vol. 156, pp. 7–20, 2019.

[11] H. R. Lee, H. Y. Kim, J. H. Jeon, and Y. J. Kang, "Application of global sensitivity analysis to statistical energy analysis: Vehicle model development and transmission path contribution," *Applied Acoustics*, vol. 146, pp. 368–389, 2019.

[12] J.-L. Christen, M. Ichchou, B. Troclet, O. Bareille, and M. Ouisse, "Global sensitivity analysis of analytical vibroacoustic transmission models," *Journal of Sound and Vibration*, vol. 368, pp. 121–134, 2016.

[13] J.-L. Christen, M. Ichchou, B. Troclet, O. Bareille, and M. Ouisse, "Global sensitivity analysis and uncertainties in sea models of vibroacoustic systems," *Mechanical Systems and Signal Processing*, vol. 90, pp. 365–377, 2017.

[14] G. B. Humphrey, H. R. Maier, W. Wu, N. J. Mount, G. C. Dandy, R. J. Abrahart, and C. W. Dawson, "Improved validation framework and r-package for artificial neural network models," *Environmental Modelling & Software*, vol. 92, pp. 82–106, 2017.

[15] S. Razavi, A. Jakeman, A. Saltelli, C. Prieur, B. Iooss, E. Borgonovo, E. Plischke, S. L. Piano, T. Iwanaga, W. Becker *et al.*, "The future of sensitivity analysis: An essential discipline for systems modeling and policy support," *Environmental Modelling & Software*, vol. 137, p. 104954, 2021.

[16] L. Breiman, "Random forests," *Machine learning*, vol. 45, no. 1, pp. 5–32, 2001.

[17] W. Chai, A. Saidi, A. Zine, C. Droz, W. You, and M. Ichchou, "Comparison of uncertainty quantification process using statistical and data mining algorithms," *Structural and Multidisciplinary Optimization*, vol. 61, no. 2, pp. 587–598, 2020.

[18] B. Sudret, "Global sensitivity analysis using polynomial chaos expansions," *Reliability engineering & system safety*, vol. 93, no. 7, pp. 964–979, 2008.

[19] A. Marrel, B. Iooss, B. Laurent, and O. Roustant, "Calculations of sobol indices for the gaussian process metamodel," *Reliability Engineering & System Safety*, vol. 94, no. 3, pp. 742–751, 2009.

[20] G. Louppe, L. Wehenkel, A. Sutera, and P. Geurts, "Understanding variable importances in forests of randomized trees," *Advances in neural information processing systems*, vol. 26, 2013.

[21] M. Jaxa-Rozen and J. Kwakkel, "Tree-based ensemble methods for sensitivity analysis of environmental models: A performance comparison with sobol and morris techniques," *Environmental Modelling & Software*, vol. 107, pp. 245–266, 2018.

[22] J. Willard, X. Jia, S. Xu, M. Steinbach, and V. Kumar, "Integrating scientific knowledge with machine learning for engineering and environmental systems," *arXiv preprint arXiv:2003.04919*, 2020.

[23] N. Zobeiry and K. D. Humfeld, "A physics-informed machine learning approach for solving heat transfer equation in advanced manufacturing and engineering applications," *Engineering Applications of Artificial Intelligence*, vol. 101, p. 104232, 2021.

[24] H. Vaddireddy, A. Rasheed, A. E. Staples, and O. San, "Feature engineering and symbolic regression methods for detecting hidden physics from sparse sensor observation data," *Physics of Fluids*, vol. 32, no. 1, p. 015113, 2020.

[25] S. Liu, B. B. Kappes, B. Amin-ahmadi, O. Benafan, X. Zhang, and A. P. Stebner, "Physics-informed machine learning for composition–process–property design: Shape memory alloy demonstration," *Applied Materials Today*, vol. 22, p. 100898, 2021.

[26] B. Cunha, A.-M. Zine, M. Ichchou, C. Droz, and S. Foulard, "On machine learning-driven surrogates for sound transmission loss simulations," *arXiv preprint arXiv:2204.12290*, 2022.

[27] I. M. Sobol, "Global sensitivity indices for nonlinear mathematical models and their monte carlo estimates," *Mathematics and computers in simulation*, vol. 55, no. 1-3, pp. 271–280, 2001.

[28] E. Borgonovo and E. Plischke, "Sensitivity analysis: a review of recent advances," *European Journal of Operational Research*, vol. 248, no. 3, pp. 869–887, 2016.

[29] A. Saltelli, P. Annoni, I. Azzini, F. Campolongo, M. Ratto, and S. Tarantola, "Variance based sensitivity analysis of model output. design and estimator for the total sensitivity index," *Computer physics communications*, vol. 181, no. 2, pp. 259–270, 2010.

[30] A. Saltelli, S. Tarantola, and K.-S. Chan, "A quantitative model-independent method for global sensitivity analysis of model output," *Technometrics*, vol. 41, no. 1, pp. 39–56, 1999.

[31] E. Scornet, "Trees, forests, and impurity-based variable importance," *arXiv:2001.04295*, 2020.

[32] F. J. Fahy and P. Gardonio, *Sound and structural vibration: radiation, transmission and response*. Elsevier, 2007.

[33] L. Cremer and M. Heckl, *Structure-borne sound: structural vibrations and sound radiation at audio frequencies*. Springer Science & Business Media, 2013.

[34] S. Narayanan and R. Shanbhag, "Sound transmission through a damped sandwich panel," *Journal of Sound and Vibration*, vol. 80, no. 3, pp. 315–327, 1982.

[35] J. Herman and W. Usher, "SALib: An open-source python library for sensitivity analysis," *The Journal of Open Source Software*, vol. 2, no. 9, jan 2017. [Online]. Available: https://doi.org/10.21105/joss.00097